
Performance Evaluation of the microPET Focus: A Third-Generation microPET Scanner Dedicated to Animal Imaging

Yuan-Chuan Tai, PhD¹; Ananya Ruangma, PhD¹; Douglas Rowland, PhD¹; Stefan Siegel, PhD²; Danny F. Newport, PhD²; Patrick L. Chow, MS³; and Richard Laforest, PhD¹

¹Department of Radiology, Washington University School of Medicine, St. Louis, Missouri; ²Concorde Microsystems, Inc., Knoxville, Tennessee; and ³Department of Molecular and Medical Pharmacology, Crump Institute for Molecular Imaging, UCLA, Los Angeles, California

The microPET Focus is the latest generation microPET system dedicated to high-resolution animal imaging and incorporates several changes to enhance its performance. This study evaluated the basic performance of the scanner and compared it with the Primate (P4) and Rodent (R4) models. **Methods:** The system consists of 168 lutetium oxyorthosilicate (LSO) detectors arranged in 4 contiguous rings, with a 25.8-cm diameter and a 7.6-cm axial length. Each detector consists of a 12 × 12 LSO crystal array of 1.51 × 1.51 × 10.00 mm³ elements. The scintillation light is transmitted to position-sensitive photomultiplier tubes via optical fiber bundles. The system was evaluated for its energy and spatial resolutions, sensitivity, and noise equivalent counting rate. Phantoms and animals of varying sizes were scanned to evaluate its imaging capability. **Results:** The energy resolution averages 18.5% for the entire system. Reconstructed image resolution is 1.3-mm full width at half maximum (FWHM) at the center of field of view (CFOV) and remains under 2 mm FWHM within the central 5-cm-diameter FOV in all 3 dimensions. The absolute sensitivity of the system is 3.4% at the CFOV for an energy window of 250–750 keV and a timing window of 10 ns. The noise equivalent counting-rate performance reaches 645 kcps for a mouse-size phantom using 250- to 750-keV and 6-ns settings. Emission images of a micro-Derenzo phantom demonstrate the improvement in image resolution compared with previous models. Animal studies exhibit the capability of the system in studying disease models using mouse, rat, and nonhuman primates. **Conclusion:** The Focus has significantly improved performance over the previous models in all areas evaluated. This system represents the state-of-the-art scintillator-based animal PET scanner currently available and is expected to advance the potential of small animal PET.

Key Words: microPET; animal PET scanner; instrumentation; performance evaluation

J Nucl Med 2005; 46:455–463

Received Apr. 5, 2004; revision accepted Oct. 8, 2004.
For correspondence contact: Yuan-Chuan Tai, PhD, Washington University School of Medicine, Campus Box 8225, 510 S. Kingshighway Blvd., St. Louis, MO 63110.
E-mail: taiy@wustl.edu

Recent advances in small animal imaging have provided new ways to perform biologic research. These nondestructive, in vivo imaging techniques permit longitudinal studies of the same animals over an extended period of time. With individual animals serving as their own control, the number of animals required for a study can be significantly reduced while the intersubject variability is minimized. Animal models may be studied with higher accuracy in less time, providing critical advantages for biomedical research and pharmaceutical development (1). Among the myriad of imaging techniques, PET provides quantitative measurements of the spatial and temporal distributions of radiolabeled molecules within living subjects. Its ability to track trace amounts of molecules within small animals offers tremendous opportunities for researchers to study normal development of biologic systems, initiation and progression of disease states, gene expression, and the pharmacokinetics or pharmacodynamics of new drugs (2,3).

Advancements in molecular biology have made genetically modified mice the animal of choice to study models of human disease. By inserting or knocking out specific genes, these transgenic mice exhibit phenotypes that are susceptible or immune to human disease. Individual risk factors can be studied to establish disease correlation as well as to develop new treatments. To better study laboratory mice using PET, researchers continue to develop new techniques to improve the performance of animal scanners, with particular emphasis on the image resolution and system sensitivity (4–15).

The microPET Focus is the latest generation of commercial microPET scanner from Concorde Microsystems, Inc. This system incorporates several changes in design that significantly improve its performance compared with previous models (16,17). This work presents an investigation into the improvement in technology and performance of the Focus system compared with the previous microPET systems.

MATERIALS AND METHODS

System Description

The Focus inherits the fundamental design and geometry of its predecessor, P4 (Primate model), with particular efforts devoted to the redesign of detector modules and pulse processing electronics. The system consists of 168 lutetium oxyorthosilicate (LSO) detectors arranged in 4 contiguous rings with a ring diameter of 25.8 cm and an axial extent of 7.6 cm. Each detector consists of a 12×12 array of LSO crystal elements coupled to a position-sensitive photomultiplier tube via an optical fiber bundle. Each LSO crystal measures $1.51 \times 1.51 \times 10.00$ mm³. Thin reflective material envelops the LSO crystals on all, but one, sides to improve the light collection efficiency and to provide better optical isolation between adjacent elements. The crystal pitch is 1.59 mm in both axial and transverse directions, resulting in a packing fraction of over 91% for a detector block.

The fiber optic bundle consists of 8×8 elements of square, multiclad plastic fibers each measuring $2.2 \times 2.2 \times 100.0$ mm³. The same reflective material is also placed between individual fibers to provide optical isolation and to improve light collection efficiency. The use of optical fibers of cross-section greater than that of the LSO elements improves the light collection efficiency. These design changes were critical for good energy resolution as the LSO crystals have a relatively small cross-section that limits the light collection efficiency (18,19).

The position-sensitive photomultiplier tube continues to be the Hamamatsu R5900-C12. A simple resistor network was used to convert the 12 anode outputs to 4 position-encoded signals (20). These 4 signals are fed into the pulse processing circuits and subsequently sent to the coincidence processor for coincidence determination. To improve the linearity of the analog-to-digital converters, each event is digitized twice and averaged for event

positioning and energy determination. The new electronics doubles the data transfer speed and effectively doubles the counting capability of the system under high counting rate situations.

The system acquires data in list mode to permit maximum flexibility in the postprocessing and reconstruction. Coincidence events can be sorted into 3-dimensional (3D) sinograms with different combinations of span and ring differences (21) or directly into 2-dimensional (2D) sinograms by single-slice rebinning (SSRB) (22). Images can be reconstructed using filtered back-projection (FBP) or ordered-subsets expectation maximization (23) (OSEM) algorithms.

The system is equipped with a point source rotating mechanism that is used to acquire a normalization scan for system calibration and transmission scans for attenuation correction. The horizontal and vertical motion of the animal bed is computer controlled, and there is a laser-positioning marker. The animal port has an opening of 22 cm to accommodate laboratory primates. The system occupies a small footprint (130×140 cm²) and comes on casters so that it can be easily moved between laboratories. Table 1 summarizes the system parameters of the Focus scanner as well as the previous microPET systems for comparison.

Energy Resolution

The system was set to acquire data in singles mode with its energy window wide open (153–814 keV). A ⁶⁸Ge point source was placed at the center of the field of view (CFOV) to acquire a 2D position histogram of each detector. Lookup tables that map locations in the flood images into crystal identifications in LSO arrays were created using system software. The same ⁶⁸Ge source was used to acquire 500 million events (~20,000 per crystal element) that were sorted by pulse height and crystal identification to provide energy spectra of individual crystals. The energy reso-

TABLE 1
Specifications of microPET Systems

Category	Parameter	Concorde Focus	Concorde P4	Concorde R4	Prototype microPET	microPET II
Detector	Crystal material	LSO	LSO	LSO	LSO	LSO
	Crystal size (mm)	$1.51 \times 1.51 \times 10.00$	$2.2 \times 2.2 \times 10.0$	$2.2 \times 2.2 \times 10.0$	$2 \times 2 \times 10$	$0.975 \times 0.975 \times 12.500$
	Crystal pitch (mm)	1.59	2.45	2.45	2.25	1.15
	Crystal array	144 (12×12)	64 (8×8)	64 (8×8)	64 (8×8)	196 (14×14)
	Photomultiplier tube	Hamamatsu R5900-C12	Hamamatsu R5900-C12	Hamamatsu R5900-C12	Philips XP1722, 64 channel	Hamamatsu H7546-M64
System	No. of detectors	168	168	96	30	90
	No. of crystals	24,192	10,752	6,144	1,920	17,640
	No. of rings	48	32	32	8	42
	No. of crystals/ring	504	336	192	240	420
	Ring diameter (cm)	25.8	26.1	14.8	17.2	16.0
	Gantry aperture (cm)	22.0	22.0	13.0	16.0	15.3
	Axial FOV (cm)	7.6	7.8	7.8	1.8	4.9
	Transaxial FOV (cm)	19.00	19.00	9.40	11.25	8.00
Dataset	No. of sinograms					
	3D	2,304	1,024	1,024	64	1,764
	2D	95	63	63	Not used	83
	Sinogram size	288×252	192×168	84×96	100×120	140×210
	Dataset size (MB)					
	3D	638	126	33	1.54	207
	2D	26.3	7.8	2.0	Not used	9.7
Sampling distance (mm)	0.795	1.225	1.225	1.125	0.575	

lution, defined as the full width at half maximum (FWHM) of the photopeak divided by the energy corresponding to the center of photopeak, was determined for each crystal in the system and the average energy resolution was calculated.

Spatial Resolution

All spatial resolution measurements were acquired with an energy window of 250–750 keV and a timing window of 6 ns using a ^{22}Na point source with a nominal size of 0.5 mm, embedded in a Lucite disk (North American Scientific). ^{22}Na has emission energy ($E_{\text{ave}}\beta^+ = 250$ keV) and positron range (~ 0.23 mm) similar to ^{18}F , the most widely used positron-emitting isotope. Results of the spatial resolution measurements were not corrected for source dimension, positron range, or acolinearity of positron annihilation.

The point source was attached to the animal bed, positioned at the CFOV, and moved radially toward the edge of the gantry opening in steps. List mode data at each location were sorted into 3D sinograms with the delayed events subtracted from the prompt events to correct for the random coincidences, followed by normalization to compensate for the differences in detection efficiency. The corrected 3D sinograms were Fourier rebinned (FORE) (24) to form 2D sinograms and subsequently reconstructed using 2D FBP with a ramp filter cutoff at the Nyquist frequency and a $10\times$ image zoom. Tangential and radial resolutions were estimated from the horizontal and vertical profiles through the pixel with maximum intensity. Axial resolution was estimated from oversampled axial profiles by interleaving 4 measurements with the source stepped along the axial direction with a step size of 0.2 mm. The FWHM and full width at tenth maximum (FWTM) were measured from the extracted profiles by linear interpolation between 2 nearest pixels bracketing the half-values and one-tenth values, respectively.

Sensitivity

The absolute sensitivity of the camera was measured using a ^{68}Ge point source encapsulated in a stainless steel sleeve. All positrons emanating from the source were assumed to annihilate in the surrounding metallic sleeve. The activity of the point source was 1.52 MBq (41 μCi) directly measured in a dose calibrator (Capintec CRC-10). The system was set to coincidence mode with an energy window of 250–750 keV and a timing window of 6 ns. The source was stepped across the entire axial FOV in 4-mm steps. At each axial location, the source was first positioned at the center of the transverse plane and then stepped toward the edge of the gantry opening in 4-mm steps, data were acquired for 60 s, and true coincidence events were sorted into 2D sinograms. The number of true coincidences was normalized to the scan duration (60 s), divided by the source activity, and corrected for the branching ratio (0.89) of ^{68}Ge . Attenuation of the stainless steel casing was not compensated for as the activity was referenced to the dose calibrator measurement. The results were plotted against the source locations to obtain the system sensitivity profile as a function of the axial and transverse locations. The same experiment was repeated under 2 other system conditions, 250–750 keV with 10 ns and 350–650 keV with 6 ns.

Counting Rate Performance

The counting rate performance of a PET system depends on the source distribution as well as the object dimension. Since the size of animals can vary drastically in different types of studies, counting rate performance was evaluated using phantoms that simulate

the geometries of a mouse, a rat, and a monkey, the most commonly studied animals in our laboratory. The design of the phantoms was based on the National Electrical Manufacturers Association (NEMA) *NU2-2001 Performance Measurements of Positron Emission Tomographs* (25), with the phantom dimension scaled down to reflect the relative difference in object size between human and animal. Although these phantoms are an oversimplified representation of real source distributions in animals, they do cover the extreme distributions where most activity is within the imaging FOV (in a mouse study) and most activity is outside the imaging FOV (as in a monkey study).

All 3 phantoms were solid cylinders made of high-density (0.96 g/cm 3) polyethylene. The mouse-like phantom was 3 cm in diameter and 7-cm long with a 3-mm hole drilled along the entire length at a radial offset of 0.75 cm from its central axis. The rat-like phantom was similarly constructed but 6 cm in diameter and 15 cm in length, and the hole was drilled at a 1.5-cm offset from the central axis. The monkey-like phantom was 10.1 cm in diameter and 40 cm in length and had a 4.8-mm-diameter hole drilled at 2.5-cm offset from the central axis. The activity was enclosed in glass tubing to have the exact same length as the respective phantoms.

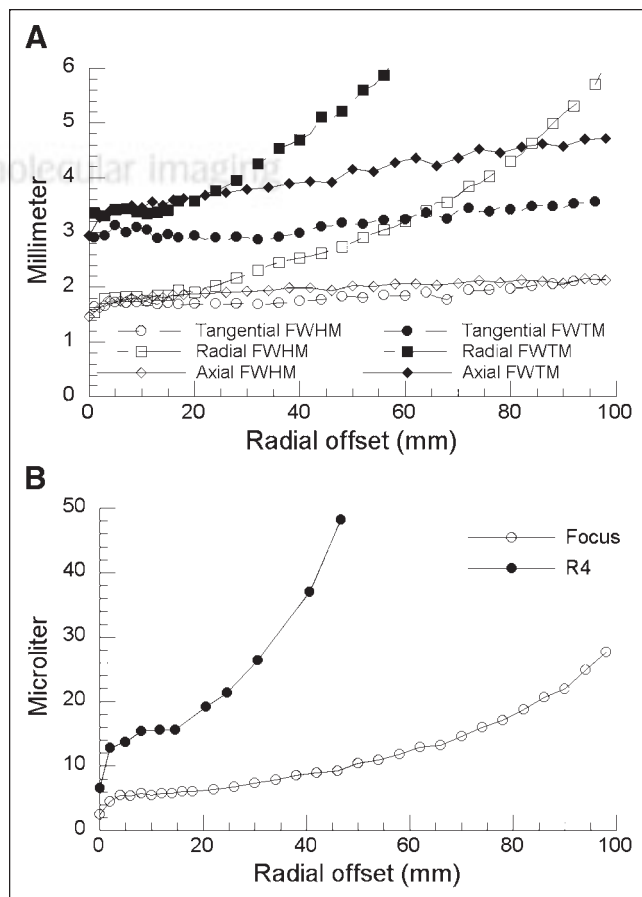


FIGURE 1. Reconstructed image resolution of microPET Focus system as function of radial offset from CFOV. (A) FWHM and FWTM of radial, tangential, and axial image resolutions were calculated by linear extrapolation of corresponding profiles extracted from point source images. (B) Volumetric resolution of the Focus compared with the R4.

For each phantom experiment, the corresponding line source was filled with >296 MBq (8 mCi) of ^{11}C before insertion into the phantom. The phantoms were centered in the tomograph and data were collected every 2–3 min for 200 min (10 half-lives) at 2 energy windows (250–750 and 350–650 keV) and 2 coincidence timing windows (6 and 10 ns). The SSRB algorithm was used to sort the list mode data into 2D sinograms. The random coincidences were measured by the delayed window technique.

The noise equivalent count (NEC) was calculated using the following formula (26):

$$NEC = \frac{T^2(1 - S_f)^2}{T + 2\alpha R}, \quad \text{Eq. 1}$$

where T is the number of true coincidences (including the scattered coincidences) calculated from the number of prompts minus the number of delayed coincidences, α is the fraction of the object in the FOV, and S_f is the fraction of events included in the trues due to scatter.

Imaging Studies

All emission studies were collected in coincidence mode using 250- to 750-keV energy and 6-ns timing window. Random coincidences were subtracted and the detector efficiencies were normalized. List mode data were sorted into 3D sinograms with a span of 3 and a maximum ring difference of 47, followed by the FORE algorithm before the reconstruction using 2D FBP. The filter used was a ramp filter cutoff at the Nyquist frequency, unless otherwise specified.

Phantom Studies. A custom-made, micro-Derenzo hot rod phantom was scanned in the Focus and the R4 (Rodent model) to visualize the improvement in image resolution. The phantom has an inner diameter of 32 mm and contains fillable hot rods of different sizes (0.80, 1.00, 1.25, 1.50, 2.00, and 2.50 mm) arranged into 6 segments. The spacing between adjacent rods in each segment is twice the rod diameter. The length of the rods is 25 mm. The phantom was filled with 18.5 MBq (0.5 mCi) of ^{18}F -FDG and scanned for 20 min in each scanner.

Animal Studies. An 18.7-g mouse was positioned in the gantry with its head centered in the FOV. A catheter was inserted into the jugular vein through which 17.8 MBq (0.48 mCi) of 2β - ^{11}C -carbomethoxy-3 β -(4-fluorophenyl)tropane (^{11}C -CFT) (27), in a

specific activity >37 MBq/nmol (28), were injected. List mode data were acquired for 120 min and sorted into 35 dynamic frames before the images were reconstructed.

A 363-g Sprague–Dawley rat was injected with 35.7 MBq (0.97 mCi) of ^{18}F -FDG via tail vein and 110 min was allowed for uptake before the rat was positioned in the scanner. Pediatric pads of an electrocardiogram-monitoring device, AccuSync 71 (AccuSync Medical Research Corp.), were connected to the paws of the rat. The AccuSync's standard transistor–transistor logic pulses were fed into the “Gating Input” of the Focus so that the trigger time would be inserted into the list mode data stream. The data were subsequently sorted into eight 3D sinograms representing 8 gates of the cardiac cycle. The images were reconstructed with a zoom of 3 using the OSEM algorithm. The same list mode data were also sorted into a single 3D sinogram without the gating option and reconstructed with the same parameters.

A 5.4-kg macaque monkey was positioned in the scanner with its brain centered in the FOV. The scanner was set up in singles mode using a 460- to 560-keV energy and 6-ns coincidence timing window. A 52-min transmission scan was acquired using a ^{68}Ge point source. Immediately after the start of a 120-min dynamic scan, 166 MBq (4.5 mCi) of 6- ^{18}F -fluoro-L-dopa (^{18}F -FDOPA) (29,30) were injected intravenously. List mode data of the emission scan were sorted into 31 dynamic frames. The transmission data were sorted using the SSRB algorithm and reconstructed with a Hanning filter cutoff at 50% of the Nyquist frequency. The choice of the Hanning filter over a ramp filter is 2-fold: to avoid amplification of statistical noise typically seen in transmission studies, and the resolution requirement for transmission images is not as high as that for emission images. Regions of interests were drawn on the transmission images to calculate the calibration factor that will scale down the linear attenuation coefficient of soft tissues to 0.095 cm^{-1} . The calibrated transmission images were forward projected to form 2D sinograms followed by inverse Fourier rebinning to generate a 3D attenuation correction file. The emission sinograms were normalized, corrected for attenuation and scatter (31), and reconstructed using FORE and 2D FBP.

All animal experiments were conducted in compliance with the Guidelines for the Care and Use of Research Animals established by the Animal Studies Committee at Washington University School of Medicine in St. Louis.

TABLE 2
Average Scatter Fraction of Mouse, Rat, and Monkey Phantoms

Phantom type	Energy window (keV)	Timing window (ns)	Scatter fraction (%)
Mouse body (3-cm \emptyset , 7-cm L, volume = 49.5 mL)	250–750	10	19.0
		6	19.0
	350–650	10	12.8
		6	12.7
Rat body (6-cm \emptyset , 15-cm L, volume = 424 mL)	250–750	10	36.5
		6	36.4
	350–650	10	27.6
		6	27.4
Monkey body (10.1-cm \emptyset , 40-cm L, volume = 3,205 mL)	250–750	10	57.6
		6	58.1
	350–650	10	40.9
		6	40.9

\emptyset = diameter; L = length.

RESULTS

Energy Resolution

Energy resolution of the 511-keV photopeak averages 18.5% for the entire system (24,192 LSO crystals). Compared with the previously reported 26% (16) and 23% (17) for the microPET P4 and R4, the energy resolution of the Focus is significantly improved despite its smaller crystal dimension.

Spatial Resolution

Figure 1A shows the radial, tangential, and axial components of the reconstructed image resolution. At the CFOV, the image resolution is 1.30-mm FWHM for both radial and tangential directions and 1.46-mm FWHM for the axial direction. All 3 components remain well under 1.80-mm FWHM within 1.0-cm radial offset (2-cm FOV). The tangential component remains below 1.86-mm FWHM throughout the central imaging FOV up to a radial offset of 60 mm. The axial component remains below 2.06-mm FWHM up to a radial offset of 60 mm. The radial component increases at a higher rate, due to depth of interaction effects, to 1.90-, 2.53-, and 3.21-mm FWHM at 20-, 40-, and 60-mm radial offsets, respectively. Volumetric resolution, defined as the product of all 3 image resolution components of a system, is shown in Figure 1B and compared with that of the R4. The improvement of the Focus over the R4 ranges from 2.6-fold at the CFOV (2.5 μL vs. 6.6 μL) to 3-fold at 2-cm radial offset (6.3 μL vs. 19.2 μL). At 60-mm radial offset, the Focus still has a volumetric resolution of 12.3 μL , which is better than the volumetric resolution of the R4 everywhere except at the very center.

Sensitivity

The sensitivity of the system as a function of transaxial and axial locations has a profile resembling a horse saddle shape, as reported previously (32). Changing the system energy and timing windows from 250–750 keV and 10 ns to 250–750 keV and 6 ns and, finally, to 350–650 keV and 6 ns, a drop in the peak absolute system sensitivity at the CFOV is seen: 3.4% to 3.0% to 2.1%, respectively.

Counting Rate Performance

The projection fraction (α) of the mouse, rat, and monkey phantoms is 0.128, 0.256, and 0.430, respectively. The average scatter fraction of all 12 experiments calculated from the sinogram slices within the central 6-cm section of the axial FOV is listed in Table 2. The scatter fraction of the mouse, rat, and monkey phantoms ranges from 12.7% to 19.0%, from 27.4% to 36.5%, and from 40.9% to 58.1%, respectively.

The NEC rates of the 3 phantoms are plotted against total activity in Figure 2 for different energy and timing windows. The system reaches its peak NEC rate of 645 kcps at 146.7 MBq (3.96 mCi) of activity in the mouse-size phantom using an energy window of 250–750 keV and a timing window of 6 ns. The peak NEC rate for the rat-size phantom is 177 kcps with a 250- to 750-keV energy window and 6-ns

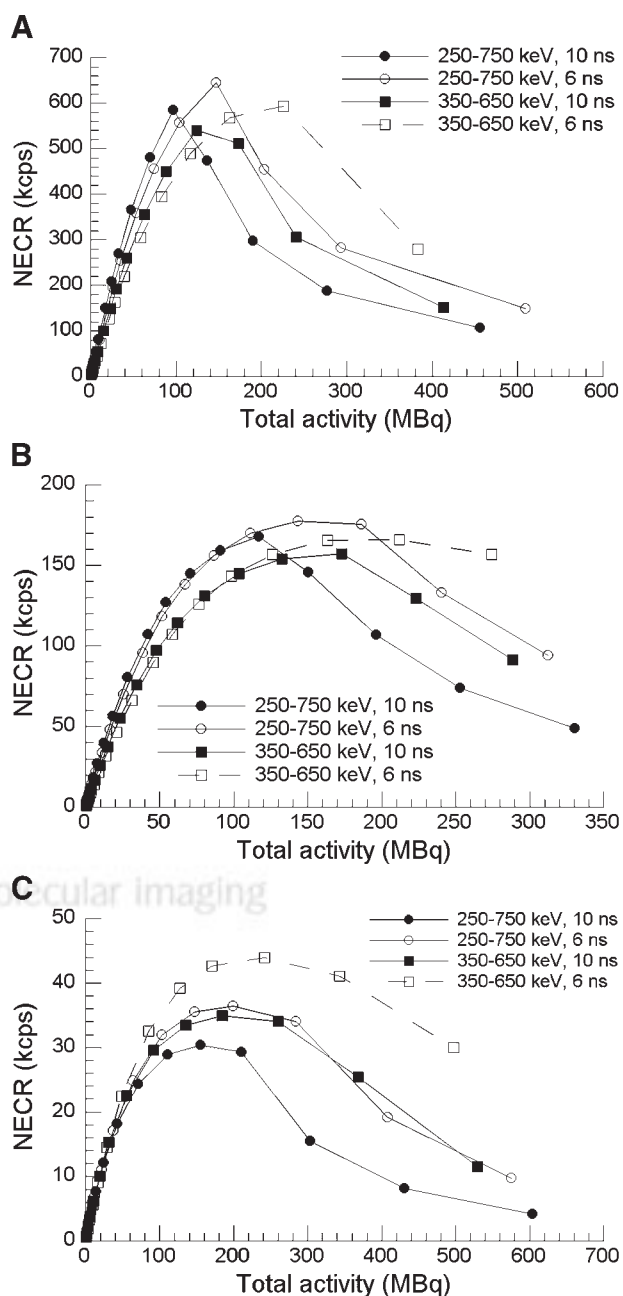


FIGURE 2. NEC rate of mouse (A), rat (B), and monkey (C) phantoms. Peak NEC rate of 645 kcps is reached with setting of 250–750 keV and 6 ns for mouse phantom. With rat phantom, peak NEC rate is 177 kcps with 250–750 keV and 6 ns. With monkey phantom, peak NEC rate is 44 kcps with 350–650 keV and 6 ns. NECR = NEC rate.

timing window when 143 MBq (3.87 mCi) of activity remained in the 15-cm tube. The peak NEC rate for the monkey-size phantom is 44.0 kcps with a 350- to 650-keV energy window and 6-ns timing window when 242 MBq (6.54 mCi) of activity remained in the 40-cm tube.

Imaging Studies

Phantom Studies. Figure 3 shows the emission images of the micro-Derenzo hot rod phantom measured by the Focus

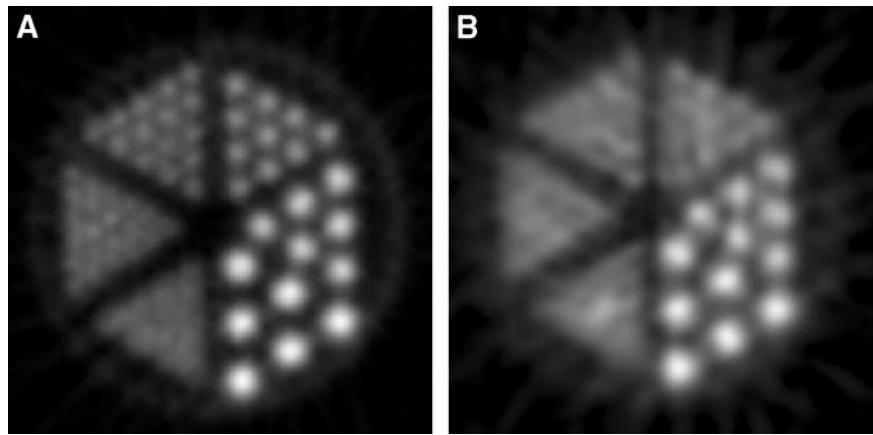


FIGURE 3. (A) Emission image measured by the Focus. (B) Same phantom as in A scanned by the R4. Diameter of rods was 0.80, 1.00, 1.25, 1.50, 2.00, and 2.50 mm, respectively. Center-to-center distance between adjacent rods was 2 times the rod diameter.

(Fig. 3A) and the R4 (Fig. 3B) systems. All 1.5-mm rods are clearly separated in the image obtained on the Focus. Rods of 1.25 mm can also be identified, although the separation between adjacent rods is less distinct. Limited by its 2-mm resolution, the R4 is not able to separate the 1.5-mm rods.

Animal Studies. Figure 4 shows the coronal image of a mouse brain using ^{11}C -CFT. The images were summed over the last 10 frames that correspond to 70–120 min after injection when most of the activity was cleared from the blood. The striatum can be clearly separated from the rest of the brain, suggesting that the resolution of the Focus might be adequate for studying the brains of transgenic mice as a model of human neurodegenerative disease.

Figure 5 shows the coronal images of a rat cardiac study with the gating feature turned on (Figs. 5A and 5B for

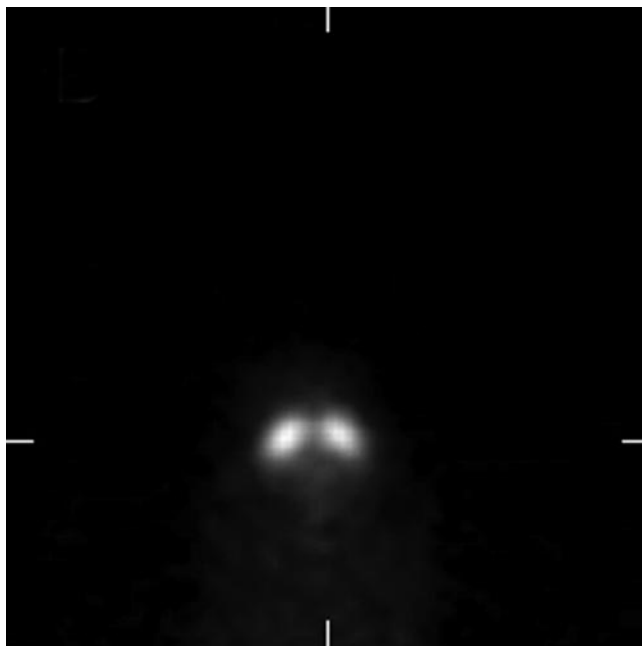


FIGURE 4. Coronal image of 18.7-g mouse injected with 17.8 MBq (0.48 mCi) of ^{11}C -CFT. Image corresponds to 50-min acquisition starting at 70 min after injection by summing the last 10 frames of 2-h dynamic study.

end-diastole and end-systole, respectively) and turned off (Fig. 5C). The left and right ventricles can be identified in the nongated image with the improved resolution of the system. The gated images provide better definition of the cardiac chambers despite lower counting statistics (approximately one eighth of the nongated images) in individual gates. Clear definition of cardiac chambers can be crucial in estimating the uptake of tracers into the myocardium, the ejection fraction of the left ventricle, and the blood input function from the left ventricle.

Figure 6 shows the transverse and coronal views of the emission (Fig. 6A) and transmission (Fig. 6B) images of a 5.4-kg macaque monkey brain using ^{18}F -FDOPA. The emission images were summed over frames 15–30 that corresponded to 40–120 min after injection. The caudate nucleus and putamen can be clearly delineated in these images. Transmission images show the air cavity in a monkey head, which cannot be estimated without a measured transmission scan.

DISCUSSION

In the design of a high-resolution animal PET system, there is often a compromise between good image resolution and high system sensitivity. Common approaches to increase the system sensitivity include the reduction of ring diameter and the use of longer detector crystal. Both approaches are subject to more severe depth-of-interaction effects that limit the usable imaging FOV or reduce the image resolution. The finer sampling and higher packing fraction of the Focus detector improve both image resolution and sensitivity compared with previous microPET models. This increase in sensitivity is critically important to support the improved image resolution in order to preserve good counting statistics without extending the acquisition time.

The option of adjusting the energy window according to the animal size permits the user to optimize the acquisition protocol for different types of studies. For a rodent study that has a small amount of intrasubject scatter, the energy window can be set wider to accept events that undergo a

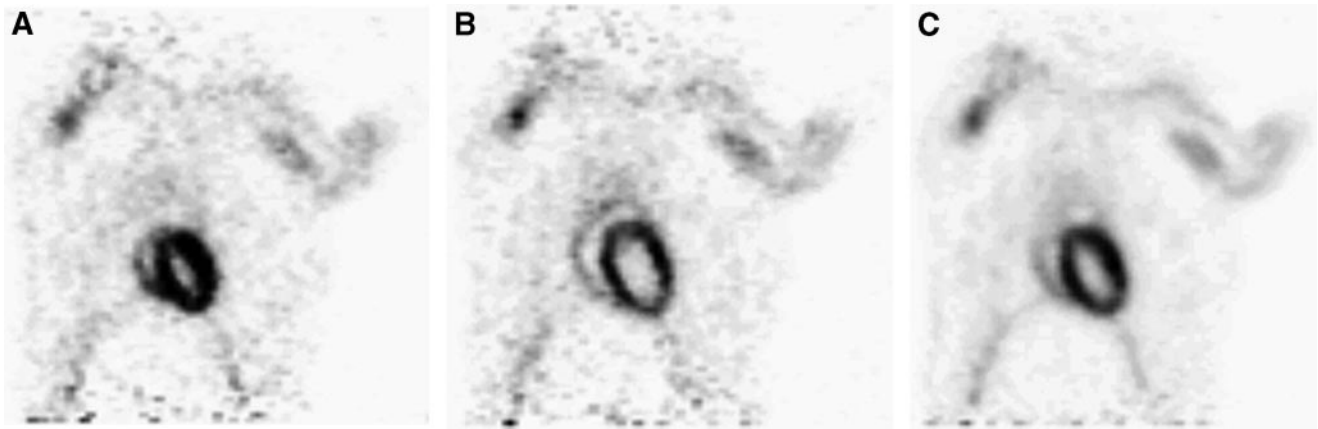


FIGURE 5. Cardiac-gated study of 363-g Sprague–Dawley rat injected with 35.7 MBq (0.97 mCi) of ^{18}F -FDG. Acquisition time was 30 min started 110 min after injection. Coronal image of heart: (A) gated at end-systole, (B) gated at end-diastole, and (C) nongated.

single Compton interaction in the LSO crystals but still describe the correct line of response. When the subject is a primate, the amount of intrasubject scatter may be high enough to warrant a narrower energy window to reduce the scatter contribution to the final image. This is reflected in the system counting rate performance study using a monkey phantom where the highest NEC rate is achieved with a tighter energy window (350–650 keV) and a tighter timing window (6 ns).

Due to the attenuation of the source housing, the effective activity of the ^{68}Ge point source used in the calculation of system sensitivity was measured directly in a dose calibrator instead of decay corrected from the assayed value. The γ -rays scattered in the source housing have a good chance of being recorded in the dose calibrator but may escape

when imaged by the PET scanner. The activity presented to the PET camera may be less than that reported by the dose calibrator; therefore, the reported system sensitivity may be slightly underestimated.

For small animals such as mice, the amount of attenuation is fairly small and does not change significantly due to intersubject variability. Transmission scans are not typically performed for mouse studies at our institution. Instead, the amount of attenuation is assumed to be a constant for mouse-size objects and is factored into the system calibration to scale up the measured activity concentration. For studies involving large animals, such as primates, where the attenuation correction is critical for quantitative accuracy, we perform a transmission scan in singles mode using a smaller energy window (460–560 keV). For the medium-

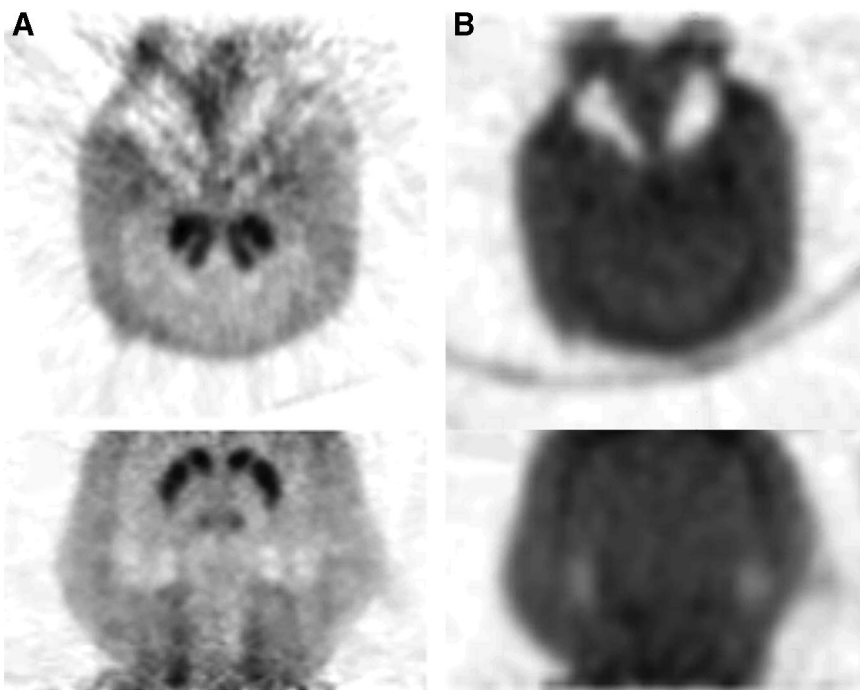


FIGURE 6. Two-hour dynamic imaging of 5.4-kg macaque monkey injected with 166 MBq (4.5 mCi) of ^{18}F -FDOPA. (A) Transverse (top) and coronal (bottom) views of emission images correspond to summed frames of 15–30 (40–120 min after injection). (B) Transmission images of monkey head of same transverse and coronal slices.

size animals such as rats, we are still evaluating the trade-offs between the use of measured attenuation correction and the use of a predetermined amount of attenuation. If the accuracy of the attenuation correction using a short transmission scan can be further improved, the measured attenuation correction may be extended to the studies using medium-size animals.

Data management is an important issue for practical use of the Focus system. A typical 30-frame dynamic study may require 13 GB of disk storage for sinograms, whereas the list mode data may only take up 1–2 GB. This has forced us to change our data archival strategy from sinograms to list mode data for all dynamic studies. To further reduce the volume of data, 2 strategies can be applied: (a) reduce the transverse imaging FOV and (b) use a larger span (21) when sorting the data into 3D sinograms. The transverse imaging FOV can be reduced by software trimming when the list mode data are sorted into sinograms. The use of larger span is known to create axial blurring toward the edge of the transverse FOV. However, if the object is a mouse or a rat centered in the gantry, the loss in resolution may be negligible.

On measuring the axial resolution as a function of radial offset using a span of 7 when sorting the 3D sinograms, the axial resolution degrades by <5% within the central 50-mm-diameter FOV compared with a span of 3. This compromise reduces the size of a 3D sinogram to less than one half that of a file rebinned using a span of 3. If we limit the transverse FOV to 5 cm and use a span of 7, then the file size drops to one tenth of the original with little degradation. This is of benefit to users who have a large number of dynamic studies using mice.

The 3D reprojection (33), 3D OSEM, and maximum a posteriori (MAP) (34) reconstruction algorithms became available from the manufacturer after this study was completed. It is expected that the more sophisticated statistical reconstruction algorithms, along with improved modeling of the physical characteristics of the system, will further improve the resolution and noise properties of the reconstructed images. Evaluation of the improvement in image resolution using these algorithms is not included in this work and will be studied in the future.

When the system was released, the calculation of the normalization file was based on a direct inversion of 3D sinograms acquired from a rotating ^{68}Ge point source. For a typical 3D sinogram that has >100 million lines of response, it is difficult to obtain high-quality normalization files with good statistics. Even with 100 GB of list mode data, the average number of counts per line of response is only slightly more than 100. Poisson statistics dictate that the variance may then be as high as 10%. A new component-based normalization procedure has been released by the manufacturer to improve the accuracy of the normalization. An initial evaluation indicates improved uniformity using this new method. The quantitative accuracy of both normalization methods, along with the accuracy of attenu-

ation, scatter, and dead time corrections, will require further investigation.

CONCLUSION

This study has evaluated the basic performance of the microPET Focus system and its improvement over previous models. Our results indicate a significant improvement in nearly all aspects of typical PET system characteristics compared with the P4 and R4 models. The energy resolution of the system averages 18.5% for the 511-keV photopeak. The volumetric image resolution remains under 12.3 μL within the central 12-cm diameter FOV, a >2.6-fold improvement compared with the P4 and the R4. The peak sensitivity is 3.4% with a 250- to 750-keV energy window and 10-ns timing window, >50% improvement over the P4. The peak NEC rate is 645 kcps with 146.7 MBq (3.96 mCi) of activity in the mouse-size phantom, >2-fold improvement over both the P4 and the R4. Imaging studies of phantoms show clear improvement in image resolution. The transmission imaging capability is now established and can be used for primate studies. The selected animal studies demonstrate that the system is capable of neurologic and cardiac studies using small rodents, as well as brain imaging of nonhuman primates. Given the improved transmission image quality, the system is expected to achieve appropriate levels of quantitation after all corrections are validated and applied.

ACKNOWLEDGMENTS

The authors thank Michael J. Welch, Arion F. Chatziioannou, Stephen Moerlein, Joel Perlmutter, Robert Mach, Terry Sharp, John Engelbach, Nicole Mercer, Lori Strong, Jerrel Rutlin, Bill Margenau, the cyclotron facility staff of Washington University School of Medicine, and Robert Nutt, Rhonda Goble, Anne Smith, Charles Landen, Aaron McFarland, R. Scott Beach, and Michael Tjon of Concorde Microsystems for valuable discussions and technical support. This work was supported by grants from the National Institutes of Health (P01-HL13851), National Cancer Institute (WUSAIR R24-CA83060 and R24-CA92865), and the Department of Energy (DE FC03-02ER63420).

REFERENCES

1. Weissleder R, Mahmood U. Molecular imaging. *Radiology*. 2001;219:316–333.
2. Phelps ME. Inaugural article: positron emission tomography provides molecular imaging of biological processes. *Proc Natl Acad Sci USA*. 2000;97:9226–9233.
3. Cherry SR, Gambhir SS. Use of positron emission tomography in animal research. *Inst Lab Anim Resources J*. 2001;42:219–232.
4. Bloomfield PM, Myers R, Hume SP, Spinks TJ, Lammertsma AA, Jones T. Three-dimensional performance of a small-diameter positron emission tomograph. *Phys Med Biol*. 1997;42:389–400.
5. Chatziioannou A, Tai YC, Doshi N, Cherry SR. Detector development for microPET II: a 1 μL resolution PET scanner for small animal imaging. *Phys Med Biol*. 2001;46:2899–2910.
6. Cherry SR, Shao Y, Silverman RW, et al. MicroPET: a high resolution PET scanner for imaging small animals. *IEEE Trans Nucl Sci*. 1997;44:1161–1166.
7. Correia JA, Burnham CA, Kaufman D, Fischman AJ. Development of a small animal PET imaging device with resolution approaching 1 mm. *IEEE Trans Nucl Sci*. 1999;46:631–635.

8. Del Guerra A, Di Domenico G, Scandola M, Zavattini G. YAP-PET: first results of a small animal positron emission tomograph based on YAP:Ce finger crystals. *IEEE Trans Nucl Sci.* 1998;45:3105–3108.
9. Huber JS, Moses WW. Conceptual design of a high-sensitivity small animal PET camera with 4 pi coverage. *IEEE Trans Nucl Sci.* 1999;46:498–502.
10. Jeavons AP, Chandler RA, Dettmar CAR. A 3D HIDAC-PET camera with sub-millimetre resolution for imaging small animals. *IEEE Trans Nucl Sci.* 1999;46:468–473.
11. Murayama H, Ishibashi I, Uchida H, Omura T, Yamashita T. Depth encoding multichannel detectors for PET. *IEEE Trans Nucl Sci.* 1998;45:1152–1157.
12. Seidel J, Vaquero JJ, Green MV. Resolution uniformity and sensitivity of the NIH ATLAS small animal PET scanner: comparison to simulated LSO scanners without depth-of-interaction capability. *IEEE Trans Nucl Sci.* 2003;50:1347–1350.
13. Tai Y, Chatziioannou A, Yang Y, et al. MicroPET II: design, development and initial performance of an improved microPET scanner for small-animal imaging. *Phys Med Biol.* 2003;48:1519–1537.
14. Weber S, Bauer A, Herzog H, et al. Recent results of the TierPET scanner. *IEEE Trans Nucl Sci.* 2000;47:1665–1669.
15. Ziegler SI, Pichler BJ, Boening G, et al. A prototype high-resolution animal positron tomograph with avalanche photodiode arrays and LSO crystals. *Eur J Nucl Med.* 2001;28:136–143.
16. Tai YC, Chatziioannou A, Siegel S, et al. Performance evaluation of the microPET P4: a PET system dedicated to animal imaging. *Phys Med Biol.* 2001;46:1845–1862.
17. Knoess C, Siegel S, Smith A, et al. Performance evaluation of the microPET R4 PET scanner for rodents. *Eur J Nucl Med Mol Imaging.* 2003;30:737–747.
18. Cherry SR, Shao Y, Tornai MP, Siegel S, Ricci AR, Phelps ME. Collection of scintillation light from small BGO crystals. *IEEE Trans Nucl Sci.* 1995;42:1058–1063.
19. Huber JS, Moses WW, Andreaco MS, Loope M, Melcher CL, Nutt R. Geometry and surface treatment dependence of the light collection from LSO crystals. *Nucl Instrum Methods [A].* 1999;437:374–380.
20. Siegel S, Silverman RW, Yiping S, Cherry SR. Simple charge division readouts for imaging scintillator arrays using a multi-channel PMT. *IEEE Trans Nucl Sci.* 1996;43:1634–1641.
21. Bendriem B, Townsend DW, eds. *The Theory and Practice of 3D PET.* Dordrecht, The Netherlands: Kluwer Academic; 1998.
22. Daube-Witherspoon ME, Muehlethner G. Treatment of axial data in three-dimensional PET. *J Nucl Med.* 1987;28:1717–1724.
23. Hudson HM, Larkin RS. Accelerated image reconstruction using ordered subsets of projection data. *IEEE Trans Med Imaging.* 1994;13:601–609.
24. Defrise M, Kinahan PE, Townsend DW, Michel C, Sibomana M, Newport DF. Exact and approximate rebinning algorithms for 3-D PET data. *IEEE Trans Med Imaging.* 1997;16:145–158.
25. National Electrical Manufacturers Association. *NEMA Standards Publication NU2-2001: Performance Measurements of Positron Emission Tomographs.* Rosslyn, VA: NEMA; 2001.
26. Strother SC, Casey ME, Hoffman EJ. Measuring PET scanner sensitivity: relating countrates to image signal-to-noise ratios using noise equivalent counts. *IEEE Trans Nucl Sci.* 1990;37:783–788.
27. Hantraye P, Brownell AL, Elmaleh D, et al. Dopamine fiber detection by [¹¹C]-CFT and PET in a primate model of parkinsonism. *Neuroreport.* 1992;3:265–268.
28. Moerlein S, Perlmutter J, Patel P, Welch M. Preparation of [C-11]CFT for PET measurement of cerebral dopamine transport activity [abstract]. *J Am Pharm Assoc.* 2004;44:255.
29. Fowler JS, Wolf AP. The heritage of radiotracers for positron emission tomography. *Acta Radiol Suppl.* 1990;374:13–16.
30. Luxen A, Guillaume M, Melega WP, Pike VW, Solin O, Wagner R. Production of 6-[¹⁸F]fluoro-L-DOPA and its metabolism in vivo: a critical review. *Nucl Med Biol.* 1992;19:149–158.
31. Watson CC. New, faster, image-based scatter correction for 3D PET. *IEEE Trans Nucl Sci.* 2000;47:1587–1594.
32. Chatziioannou AF, Cherry SR, Shao Y, et al. Performance evaluation of microPET: a high-resolution lutetium oxyorthosilicate PET scanner for animal imaging. *J Nucl Med.* 1999;40:1164–1175.
33. Kinahan PE, Rogers JG. Analytic 3D image reconstruction using all detected events. *IEEE Trans Nucl Sci.* 1989;36:964–968.
34. Qi J, Leahy RM, Cherry SR, Chatziioannou A, Farquhar TH. High-resolution 3D Bayesian image reconstruction using the microPET small-animal scanner. *Phys Med Biol.* 1998;43:1001–1013.

